Chemical Geology 402 (2015) 40–51

Contents lists available at ScienceDirect

Chemical Geology

journal homepage: www.elsevier.com/locate/chemgeo

Experimental constraints on kinetic and equilibrium silicon isotope fractionation during the formation of non-biogenic chert deposits

Desiree L. Roerdink [a,b,*], Sander H.J.M. van den Boorn [a,1], Sonja Geilert [a,2], Pieter Z. Vroon [c], Manfred J. van Bergen [a]

[a] Department of Earth Sciences, Utrecht University, Budapestlaan 4, 3584 CD Utrecht, The Netherlands
[b] Centre for Geobiology, Department of Earth Sciences, University of Bergen, Allégaten 41, N-5007 Bergen, Norway
[c] Department of Petrology, VU University, De Boelelaan 1085, 1081 HV Amsterdam, The Netherlands

ARTICLE INFO

Article history:
Received 9 September 2014
Received in revised form 16 January 2015
Accepted 27 February 2015
Available online 7 March 2015

Edited by: Michael E. Böttcher

Keywords:
Silicon isotope fractionation
Amorphous silica precipitation
Batch-reactors
Non-biogenic chert

ABSTRACT

Silicon isotopic compositions ($\delta^{30}Si$) of modern and ancient siliceous sedimentary rocks provide valuable information on conditions in depositional environments, but interpretations are hampered by the lack of experimentally validated fractionation factors. Here, we present new constraints on the magnitudes of kinetic and equilibrium isotope effects during chemical precipitation of amorphous silica in batch-reactors at low temperature (10–35 °C) and near-neutral pH (7.5–8.5), as analogue for non-biogenic chert formation. Instantaneous fractionation factors, derived from $\delta^{30}Si$-values of the total dissolved (Si_{TD}) silica and mass balance computations with $\alpha_{inst} = (\delta^{30}Si_{ppt} + 1000)/(\delta^{30}Si_{TD} + 1000)$, decrease with progressive precipitation and reduced reaction rates. This suggests that silica deposition in the batch-reactors is kinetically-dominated at the start of the experiments but approaches a metastable equilibrium after *ca.* 400 hours. Modelled kinetic fractionation factors range from 0.9965 at 10 °C, to 0.9976 at 20 °C and 0.9993 at 35 °C and pH 8.5, whereas equilibrium isotope effects are smaller and range from 0.9995 at 10 °C, to 1.000 at 20 °C and 1.0005 at 35 °C. Our results suggest that large isotope effects are only expressed in natural systems where dissolved and precipitated silica are not equilibrated, implying that the kinetic conditions of non-biogenic silica precipitation provide important constraints on silicon isotope ratios of siliceous rocks, with particular relevance for those preserved in the Archean chert record.

1. Introduction

Silicon isotopic compositions (^{28}Si, ^{29}Si, ^{30}Si) of siliceous sedimentary rocks provide valuable information on the marine geochemical silica cycle throughout geological history. Chemical and biological exchange reactions between dissolved silica in seawater and biogenic or inorganic silica precipitates produce small but measurable isotope fractionation, resulting in a natural range in $^{30}Si/^{28}Si$ ratios ($\delta^{30}Si$) from *ca.* −3‰ to +3‰ in the marine environment (Douthitt, 1982; Ding et al., 1996). Since Mesozoic times, the silicon isotopic composition of seawater and opaline sediments is largely controlled by biological fractionation during silica uptake by diatoms (Tréguer et al., 1995). Magnitudes of isotope fractionation in marine diatoms are well-constrained by experimental work (De La Rocha et al., 1997; Demarest et al., 2009; Sutton et al., 2013), so that isotope ratios of biogenic silica can be used to reconstruct past ocean productivity and silicic acid utilization in paleoclimatic and paleoceanographic studies (De La Rocha et al., 1998; De La Rocha and Bickle, 2005; De La Rocha, 2006; Egan et al., 2012).

In contrast, in the Archean oceans and before the evolution of silica-secreting organisms, fractionation of silicon isotopes was limited to abiotic processes. Due to a significant hydrothermal source and a lack of biogenic sinks, dissolved silica concentrations in seawater were probably well above opal solubility levels (~120 ppm or 2 mmol L^{-1} SiO_2 at 25 °C; Gunnarsson and Arnórsson, 2000), resulting in direct precipitation of amorphous silica from seawater and the formation of ubiquitous chert deposits (Siever, 1991). Consequently, the silicon isotopic composition of these cherts is likely to reflect ambient conditions in the early marine environment. Previous work demonstrated a significant variability in silicon isotope ratios in Archean cherts ($\delta^{30}Si = -4.3‰$ to +2.9‰), which was explained by variable silica sources and hydrothermal inputs, seawater temperatures as well as different mechanisms of isotope fractionation and Rayleigh distillation during silica precipitation (Robert and Chaussidon, 2006; Van den Boorn et al., 2007; Steinhoefel et al., 2009; Van den Boorn et al., 2010; Abraham et al., 2011; Heck et al., 2011; Marin-Carbonne et al., 2011; Chakrabarti et al., 2012; Geilert et al., 2014b; Marin-Carbonne et al., 2014). However, the interpretation of these data is hampered by the

* Corresponding author. Tel.: +47 55 58 38 60.
E-mail address: desiree.roerdink@geo.uib.no (D.L. Roerdink).
[1] Present address: Shell Projects and Technologies, Kessler Park 1, 2288 GS, Rijswijk, The Netherlands.
[2] Present address: GEOMAR Helmholtz Centre for Ocean Research Kiel, Wischhofstraße 1-3, 24148 Kiel, Germany.

http://dx.doi.org/10.1016/j.chemgeo.2015.02.038
0009-2541/

limited knowledge of fractionation factors associated with abiotic silica deposition. The most negative values measured in Archean cherts were explained by sequential fractionation processes (Heck et al., 2011; Marin-Carbonne et al., 2011; 2014), because isotope effects were larger than observed in early experiments (−0.4 to −1.0‰) by Li et al. (1995). However, these experimentally determined fractionation factors are considerably smaller than the difference in isotopic composition between modern hydrothermal fluids and associated silica (−3.5‰; Douthitt, 1982; Ding et al., 1996), suggesting that the application of experimental data to natural systems may not be straightforward. Positive δ^{30}Si-values have been attributed to Rayleigh fractionation processes (Van den Boorn et al., 2010; Abraham et al., 2011; Heck et al., 2011; Chakrabarti et al., 2012), but these models also rely heavily on the magnitude of the abiotic fractionation factor. In addition, it remains unknown to what extent the observed variation in chert isotopic ratios can be explained by the conditions at which the silica precipitated and subsequently diagenetically transformed. Recent experimental work revealed that isotope fractionation during silica precipitation under steady state conditions is inversely correlated with temperature (Geilert et al., 2014a), whereas isotope effects during adsorption of silica onto gibbsite were shown to be dependent on the initial concentration of dissolved silica and adsorption rates (Oelze et al., 2014). These results suggest that the kinetic regime at which the silica precipitated provided an additional, yet unexplored control on the silicon isotopic composition of chert deposits.

In this study, we determine the fractionation of silicon isotopes during abiotic silica precipitation at different kinetic conditions in batch-reactors under controlled temperatures (10–35 °C) and pH (7.5–8.5). Our experimental set-up allows us to evaluate isotopic fractionation throughout the entire precipitation process from high degrees of oversaturation towards equilibrium conditions, using high-precision isotope analysis of the dissolved silica by multi-collector inductively-coupled plasma mass spectrometry (MC-ICP-MS). The closed-system approach enables us to use an isotopic mass balance to calculate instantaneous fractionation factors, and derive overall kinetic and equilibrium fractionation factors using the surface kinetic model of DePaolo (2011).

2. Methods

2.1. Experimental procedure

A starting solution was prepared by dissolving 10 g L^{-1} of Aerosil OX50 fumed silica particles (Evonik Industries) in ultrapure water at 90 °C until the solubility concentration of ~330 ppm SiO_2 (5.5 mmol L^{-1}) (Gunnarsson and Arnórsson, 2000) was reached (~1 week). The solution was stored in a fluorinated ethylene propylene (FEP) bottle to avoid silicon contamination from glassware. In addition to dissolved silica, the starting solution contained undissolved silica particles that acted as nucleation seeds in the batch-reactors, facilitating deposition of monomeric and/or oligomeric silica and preventing significant polymerization reactions (cf. Fleming, 1986). This approach enabled us to separate the dissolved silica from precipitated products by filtration (see Supplementary Data Section 3), and determine isotopic fractionation from the δ^{30}Si-values of the residual dissolved silica. This is not feasible for polymerization reactions since the produced silica polymers may be too small (3–30 nm, Conrad et al., 2007) to be separated from the residual silica pool by ordinary filtration techniques. In addition, isotopic analysis of the solid phase is not possible because the amount of precipitated silica (*ca.* 15 mg) is very small compared to the abundance of silica seeds (*ca.* 500 mg), so that changes in its isotopic composition are likely to be minimal and less than the analytical precision.

At the beginning of each batch-reactor experiment, the solution was shaken vigorously to ensure a uniform distribution of the undissolved silica particles, and was subsequently poured into 50 ml centrifuge

Table 1
Experimental results, with the measured concentrations of molybdate-reactive silica ($[SiO_2]_{n<3}$), total dissolved silica ($[SiO_2]_{TD}$) and isotopic compositions of the total dissolved silica ($\delta^{29}Si_{TD}$ and $\delta^{30}Si_{TD}$) relative to NBS-28 standard. The percentage of polymeric silica ($[SiO_2]_{n>3}$) was calculated from the difference between $[SiO_2]_{TD}$ and $[SiO_2]_{n<3}$ and normalized against $[SiO_2]_{TD}$. The fraction of silica remaining in solution $f(SiO_2)_{rem}$ was calculated as $[SiO_2]_{TD}/[SiO_2]_i$ where $[SiO_2]_i$ is the initial value of $[SiO_2]_{TD}$ (time = 0 hrs), ([a]) except for the sample at time t = 459 hours where $[SiO_2]_{TD}$ was assumed to be equal to $[SiO_2]_{n<3}$.

Sample	Time	$[SiO_2]_{n<3}$	$[SiO_2]_{TD}$	$[SiO_2]_{n>3}$	$f(SiO_2)_{rem}$	$\delta^{29}Si_{TD}$	$\delta^{30}Si_{TD}$
	hours	ppm SiO_2	ppm SiO_2	% of TD		‰ NBS-28	‰ NBS-28
Reactor B1, T = 19.7 ± 1.2 °C, pH = 7.3 ± 0.2							
Initial	0.0	311	339	8.2	1.00	−0.37	−0.71
B1-1	0.5	282	305	7.7	0.90	−0.10	−0.13
B1-2	2.2	253	275	7.9	0.81	0.08	0.20
B1-3	4.1	232	259	10.5	0.77	0.22	0.38
B1-4	6.1	217	238	8.8	0.70	0.18	0.36
B1-5	22.9	181	191	5.2	0.56	0.30	0.55
B1-6	48.3	154	167	8.5	0.50	0.27	0.54
B1-7	167	139	145	4.0	0.43	0.19	0.34
B1-8	459	129	-	-	[a] 0.38	0.04	0.09
Reactor B2, T = 19.4 ± 1.1 °C, pH = 8.1 ± 0.1							
Initial	0.0	309	336	8.2	1.00	−0.37	−0.71
B2-1	0.5	271	291	6.6	0.86	−0.04	−0.04
B2-2	2.1	228	245	6.8	0.73	0.16	0.37
B2-3	4.0	198	213	7.1	0.63	0.27	0.52
B2-4	6.0	180	196	7.8	0.58	0.25	0.54
B2-5	22.8	147	152	3.5	0.45	0.21	0.37
B2-6	48.3	134	144	7.1	0.43	0.06	0.16
B2-7	167	122	126	3.7	0.38	−0.13	−0.26
B2-8	459	115	-	-	[a] 0.34	−0.20	−0.47
Reactor B3, T = 19.4 ± 1.2 °C, pH = 8.6 ± 0.1							
Initial	0.0	308	335	8.2	1.00	−0.37	−0.71
B3-1	0.4	291	328	11.3	0.98	−0.03	−0.05
B3-2	2.0	201	223	9.9	0.67	0.12	0.36
B3-3	4.0	176	198	11.0	0.59	0.14	0.35
B3-4	6.0	169	180	5.7	0.54	0.13	0.20
B3-5	22.8	141	150	5.7	0.45	0.02	0.02
B3-6	48.3	134	140	4.5	0.42	−0.14	−0.21
B3-7	167	124	124	0.4	0.37	−0.30	−0.56
B3-8	459	111	-	-	[a] 0.33	−0.37	−0.75
Reactor B4, T = 10.6 ± 0.6 °C, pH = 8.7 ± 0.1							
Initial	0.0	309	337	8.2	1.00	−0.37	−0.71
B4-1	0.3	262	296	11.2	0.88	−0.09	−0.15
B4-2	1.8	209	233	10.0	0.69	0.36	0.63
B4-3	3.8	186	200	7.2	0.59	0.45	0.92
B4-4	5.9	180	180	0.1	0.53	0.47	0.98
B4-5	22.8	138	136	-	0.40	0.34	0.69
B4-6	48.1	118	124	5.0	0.37	0.21	0.37
B4-7	167	104	107	3.2	0.32	−0.05	−0.08
B4-8	459	95	-	-	[a] 0.28	−0.25	−0.44
Reactor B5, T = 34.7 ± 0.8 °C, pH = 8.5 ± 0.1							
Initial	0.0	310	338	8.2	1.00	−0.37	−0.71
B5-1	0.3	254	284	10.4	0.84	−0.09	−0.22
B5-2	1.8	207	237	12.6	0.70	−0.23	−0.42
B5-3	3.8	198	218	8.9	0.64	−0.23	−0.52
B5-4	5.9	188	213	12.0	0.63	−0.23	−0.50
B5-5	22.8	170	192	11.1	0.57	−0.36	−0.74
B5-6	48.1	171	184	7.1	0.55	−0.35	−0.70
B5-7	167	162	167	2.7	0.49	−0.47	−0.93
B5-8	459	151	-	-	[a] 0.45	−0.57	−1.11
Control reactor, T = 19.5 ± 0.7 °C, pH = 3.6 ± 0.1							
Initial	0.0	317	347	8.8			
Control-1	2.0	295	336	12.1			
Control-2	3.6	291	339	14.0			
Control-3	5.6	304	343	11.3			
Control-4	7.8	306	343	10.7			
Control-5	24.6	310	328	5.7			
Control-6	49.9	313	337	7.2			
Control-7	169	310	333	7.0			
Control-8	461	297	-	-			

tubes. The reactors were cooled down for 30 minutes to the desired temperature at 10, 20 and 35 °C in a water bath, and were alkalized with a 0.001 M NaOH solution to pH-values of *ca*. 7.5, 8.0 and 8.5 (see Table 1 for reactor conditions). As a result of the reduced silica solubility at lower temperatures (Gunnarsson and Arnórsson, 2000), dissolved silica precipitated until new solubility levels were reached. A control reactor showed that no precipitation occurred during cooling prior to the NaOH addition (Table 1), indicating sluggish reaction kinetics at the initially low pH (3.6 ± 0.1). Suspensions of silica seeds and dissolved silica were sampled from the reactors (preserving constant solid/liquid ratios throughout the experiments) at regular time intervals for both concentration and isotope analysis. After measuring the temperature and pH, a disposable syringe was used to sample a 2.5 ml aliquot from reactors, which was subsequently filtered through a 0.2 μm nylon syringe filter. Approximately 0.5 ml of the filtered solution was diluted directly into 9.5 ml of ultrapure water for concentration analysis, and the remaining 2 ml was diluted with ultrapure water to a solution containing *ca*. 110 ppm (1.83 mmol L^{-1}) SiO_2 for isotope analysis. Similar procedures were used to sample the starting solution directly from the stock bottle.

2.2. Concentration analysis

Concentrations of monomeric (H_4SiO_4), dimeric ($H_6Si_2O_7$) and possibly trimeric silica ($H_8Si_3O_{10}$), in this manuscript referred to as 'molybdate-reactive silica' or $[SiO_2]_{n<3}$ after Icopini et al. (2005), were measured by UV-spectrophotometer at 660 nm using the molybdenum blue method after Iler (1979). Samples were diluted to concentrations between 0.2 and 20 ppm SiO_2 and were analyzed in duplicate. Standard solutions with 2 and 10 ppm SiO_2 were included in each analytical session and demonstrated an average precision of 5% on spectrophotometry results. Comparison of a true blank and a blank with NaOH showed that base addition did not affect the molybdenum blue method. To verify if silica precipitation in the batch-reactors occurred via molybdate-reactive silica deposition or polymerization reactions (Iler, 1979), molybdate-reactive silica concentrations were compared with the total dissolved silica contents of solutions ($[SiO_2]_{TD}$), measured by inductively-coupled plasma atomic emission spectroscopy (Spectro Ciros ICP-AES) in acidified sample solutions with 1% HNO_3. Typical instrumental precision for Si obtained in this method was 2% (1rsd). The concentration of polymeric silica (i.e. consisting of more than 3 silica monomers) was calculated from the difference between $[SiO_2]_{TD}$ and $[SiO_2]_{n<3}$ and is referred to as $[SiO_2]_{n>3}$.

2.3. Silicon isotope analysis

To ensure matrix-matched samples and standard solutions during multi-collector inductively coupled plasma mass spectrometry (MC-ICP-MS) isotope analysis, Na-ions resulting from pH adjustments were removed from diluted reactor solutions using a BioRad AG50-X8 cation-exchange resin, following procedures described by Van den Boorn et al. (2006). These authors demonstrated that high yields (>97%) were achieved for Si on these columns, and in addition, any polymeric silica that may have been formed during sample storage should pass the column since the negatively-charged polymers are not retained on the resin. Purified solutions were acidified to 1% HNO_3, centrifuged for 3 minutes at 3000 rpm and diluted to 4 ppm Si in a 1% HNO_3 matrix. All tubes used for sample preparation were pre-cleaned with HNO_3-HF. Isotope measurements were performed with a ThermoFinnigan Neptune MC-ICP-MS at the VU University Amsterdam, using instrument settings described in Van den Boorn et al. (2006). Samples were run in static mode at medium resolution, using the Stable Introduction System (SIS) with a 50 μl nebulizer and Teflon spray chamber. Data were collected with ^{28}Si in Faraday cup L4, ^{29}Si in L1 and ^{30}Si in the center cup. We report isotopic compositions as blank-corrected isotope ratios calculated by the standard-sample bracketing method, with values of $\delta^{29}Si$ and $\delta^{30}Si$ defined relative to the NBS-28 standard following Eq. 1 (replace ^{30}Si for ^{29}Si to calculate $\delta^{29}Si$):

$$\delta^{30}Si = \left[\frac{\left(^{30}Si/^{28}Si\right)_{sample}}{\sqrt{\left(^{30}Si/^{28}Si\right)_{std-I} \times \left(^{30}Si/^{28}Si\right)_{std-II}}} - 1 \right] \times 1000 \quad (1)$$

Std-I and std-II represent the standards measured immediately before and after the unknown, respectively. A precision of 0.07‰ on $\delta^{29}Si$ (2rsd) and 0.12‰ on $\delta^{30}Si$ was obtained on the basis of repeated analyses of Diatomite standard (Supplementary Data Section 4), which is similar to the precision obtained in dry plasma mode in previous studies (De La Rocha, 2002; Cardinal et al., 2003; Van den Boorn et al., 2006; Zambardi and Poitrasson, 2011).

3. Model outline

3.1. Model outline

To quantify the isotope effect associated with silica precipitation in our batch-reactors, we use an isotopic mass balance model to calculate the isotopic composition of the precipitated silica ($\delta^{30}Si_{ppt}$) from the measured $\delta^{30}Si$-values of the total dissolved silica ($\delta^{30}Si_{TD}$) and the initial isotopic composition of the stock solution ($\delta^{30}Si_i$):

$$\delta^{30}Si_i.mSiO_{2,i} = \delta^{30}Si_{TD}.mSiO_{2,TD} + \delta^{30}Si_{ppt}.mSiO_{2,ppt} \quad (2)$$

The initial mass of SiO_2 ($mSiO_{2,i}$) as well as SiO_2 remaining in the reactor ($mSiO_{2,TD}$) were calculated from the measured concentrations of total dissolved SiO_2 (except for the sample at time t = 459 hours where $[SiO_2]_{TD}$ was assumed to be equal to $[SiO_2]_{n<3}$) and the reactor volume, taking into account that the volume was reduced with 2.5 ml for each aliquot taken. The total amount of SiO_2 precipitated ($mSiO_{2,ppt}$) was subsequently calculated for each sample by assuming a closed system and subtracting the mass of dissolved silica from the initial amount.

Instantaneous fractionation factors (α_{inst}) were calculated for each sample at time *t* from the difference in isotopic composition between the precipitated and dissolved silica, using the equation:

$$\alpha_{inst} = \frac{\left(\delta^{30}Si_{ppt} + 1000\right)}{\left(\delta^{30}Si_{TD} + 1000\right)} \quad (3)$$

Following the kinetic model for isotope fractionation during mineral precipitation by DePaolo (2011), results are plotted against silica precipitation rates (R_p in mol SiO_2 m^{-2} s^{-1}) calculated from the change in $mSiO_{2,ppt}$ over a time interval between two sampling moments ($\Delta t = t_{II} - t_I$) and the volume-corrected surface area (A) in the reactor:

$$R_p = \left(mSiO_{2,ppt\ I} - mSiO_{2,ppt\ II}\right)/(A.\Delta t) \quad (4)$$

For the stock solution with 10 g L^{-1} Aerosil OX50 particles (BET specific surface area of 50 m^2 g^{-1} as given by Evonik Industries) of which 330 ppm SiO_2 has been dissolved at 90 °C, we calculated a surface area of 483 m^2 L^{-1} that was subsequently multiplied by the reactor volume at time *t* to derive the volume-corrected surface area *A*, which takes into account that sampling of the suspension reduces the total amount of solids throughout the experiment.

Magnitudes of kinetic (α_{kin}) and equilibrium (α_{eq}) fractionation factors were determined from fitting the surface kinetic model of DePaolo (2011) to the calculated instantaneous fractionation factors (α_{inst}). Note that the obtained equilibrium fractionation factor does

not represent isotopic exchange at true thermodynamic equilibrium, but at the metastable equilibrium represented by the solubility level of amorphous silica. Nevertheless, we will refer to this fractionation factor as α_{eq} in this paper, because the principle of isotopic exchange is similar at thermodynamic and metastable equilibrium. The mathematical expression for the model is given by:

$$\alpha_{inst} = \frac{\alpha_{kin}}{1 + \frac{R_b}{R_p + R_b}\left(\frac{\alpha_{kin}}{\alpha_{eq}} - 1\right)} \quad (5)$$

where R_p is the measured precipitation rate and R_b is the backward dissolution rate. We assumed that R_b was primarily dependent on the pH of our reactor solutions and calculated rates from dissolution experiments with the same batch of Aerosil OX50 particles in fresh water at pH 6.3 and pH 8.1 (Loucaides et al., 2008). Since *log* R_b is linearly correlated with pH between pH 7 and 9 (Wirth and Gieskes, 1979; Mazer and Walther, 1994; Plettinck et al., 1994; Seidel et al., 1997), we used linear extrapolation to obtain values of R_b at pH 7.5, 8.0 and 8.5 (see Table 3). Eq. 5 can be rewritten into a linear form by taking the reciprocal:

$$\frac{1}{\alpha_{inst}} = \frac{1 + \frac{R_b}{R_p + R_b}\left(\frac{\alpha_{kin}}{\alpha_{eq}} - 1\right)}{\alpha_{kin}} \quad (6)$$

which can be simplified to the expression:

$$\frac{1}{\alpha_{inst}} = \frac{1}{\alpha_{kin}} + \frac{R_b}{R_p + R_b}\left(\frac{1}{\alpha_{eq}} - \frac{1}{\alpha_{kin}}\right) \quad (7)$$

Using Eq. 7, we calculated values of α_{kin} and α_{eq} for each batch-reactor using least squares linear regression on $1/\alpha_{inst}$ *versus* $R_b/(R_p + R_b)$. Uncertainties on the obtained fractionation factors are calculated as 95% confidence intervals (see Table 3 for results).

4. Results

4.1. Experimental results

Both molybdate-reactive silica and total silica concentrations decreased rapidly after cooling and addition of diluted NaOH to the reactor solutions (Table 1 and Fig. 1). After 20 days, molybdate-reactive silica levels were 6–23% above theoretical solubility levels of 85 ppm (1.42 mmol L^{-1}) SiO_2 at 10 °C, 105 ppm (1.75 mmol L^{-1}) at 20 °C and 140 ppm (2.33 mmol L^{-1}) at 35 °C (Gunnarsson and Arnórsson, 2000). Polymeric silica ($[SiO_2]_{n>3}$), calculated from the difference between total silica and molybdate-reactive silica concentrations, was generally less than 10% and decreased during the experimental runs, suggesting minor polymerization in addition to monomeric silica deposition.

All batch-reactor experiments showed an increase in δ^{30}Si-values of the total dissolved silica during the initial phase of the precipitation reaction down to $f \approx 0.6$, with f representing the fraction of silica remaining in solution at time t relative to the initial concentration (Table 1 and Fig. 2). The increase was largest in experiment B4 ($\Delta^{30}Si = +1.69‰$) and smallest in B5 ($\Delta^{30}Si = +0.48‰$). In contrast, after more than 40% of the available silica precipitated, the isotopic composition of the dissolved silica decreased again to δ^{30}Si-values close to the initial composition of the stock solution ($\delta^{30}Si = -0.71 \pm 0.07‰$). In experiments B3 and B5, the final δ^{30}Si-value of the total dissolved silica was more ^{30}Si-depleted than the initial stock solution, with $\delta^{30}Si = -0.75‰$ in batch-reactor experiment B3 and $\delta^{30}Si = -1.11‰$ in B5.

4.2. Model results

Instantaneous isotopic fractionation factors decrease with progressive precipitation in the batch-reactors, from *ca.* 0.9960 to values around unity when solubility levels were approached (Table 2). Relatively large fractionation effects were calculated for the first aliquots of reactors B3 (0.9907) and B5 (0.9976) compared to other values of α_{inst} for these reactors, which may be due to errors in concentration or isotope analysis that affect the mass balance. All of the instantaneous fractionation factors plot in the transition zone between kinetic isotope fractionation (the lower limit of the curve) and equilibrium effects (the upper limit of the curve) in the DePaolo (2011) model (Fig. 3). From the linear regression method outlined above, we obtained kinetic fractionation factors of 0.9967 ± 0.0005 for reactor B1, 0.9968 ± 0.0005 for reactor B2 and 0.9965 ± 0.0002 for reactor B4 (Table 3), corresponding to isotope enrichment factors ($\varepsilon = 1000\ln\alpha$) of −3.4 ± 0.5‰ for B1, −3.2 ± 0.5‰ for B2 and −3.5 ± 0.2‰ for experiment B4. Excluding the anomalously large isotope effects for the first aliquots, smaller kinetic fractionation factors were found for reactors B3 ($\alpha_{kin} = 0.9976 \pm 0.0004$, or $\varepsilon_{kin} = -2.4 \pm 0.4‰$) and B5 ($\alpha_{kin} = 0.9993 \pm 0.0002$, or $\varepsilon_{kin} = -0.7 \pm 0.2‰$). Calculated metastable equilibrium fractionation factors were close to unity and range from 0.9991 ± 0.0016 in reactor B1 ($\varepsilon_{eq} = -0.9 \pm 1.6‰$), to a value of 1.0005 ± 0.0006 ($\varepsilon_{eq} = +0.5 \pm 0.6‰$) in reactor B5 that is suggesting ^{30}Si-enrichment at isotopic equilibrium (Table 3).

5. Discussion

5.1. Mechanism of isotope fractionation

Calculated kinetic fractionation factors, as well as the ^{30}Si-enrichment of the dissolved silica during the initial stages of the experiment, confirm the preferential deposition of ^{28}Si during abiotic silica precipitation (Li et al., 1995; Geilert et al., 2014a). Similar enrichments of light isotopes in the solid phase were observed for Fe-isotopes during rapid precipitation of hematite (Skulan et al., 2002), Ca-isotopes during calcite precipitation (DePaolo, 2004) and Mg-isotopes in magnesite deposition (Pearce et al., 2012), which are assumed to be linked to diffusion, unidirectional adsorption and entrapment of ions in solution. However, mechanisms of isotope fractionation are likely (and at least partially) different for silica precipitation because dissolved silicon does not occur as ions, but as monomers, oligomers and/or polymers that cannot readily attach to a solid surface. Although low concentrations of polymeric silica ($[SiO_2]_{n>3}$) were measured in our solutions that decreased throughout the experiment (Table 2), suggesting minor deposition of polymers, several lines of evidence argue for deposition of monomeric (and/or oligomeric) silica as the dominant precipitation mechanism. First, no induction time was observed in the decrease of molybdate-reactive silica, as concentrations ($[SiO_2]_{n<3}$) decreased immediately after the onset of the experiment. This contrasts with the expected time lag of *ca.* 24 hours at pH 7–8 in decreasing levels of molybdate-reactive silica during polymerization reactions (Supplementary Data Section 1 and Rothbaum and Rohde, 1979; Weres et al., 1981). Secondly, the relative amount of polymeric silica (Table 1) is significantly lower than in polymerization experiments by Icopini et al. (2005), where polymeric silica contents were 60 to 80% of the total silica at pH 7–8. This suggests that, if polymerization was the dominant pathway of silica precipitation in our batch-reactors, significantly higher polymer levels would be expected. In addition, the same authors found very slow polymerization rates at low levels of oversaturation (4.2 mmol L^{-1} SiO_2, compared to our 5.5 mmol L^{-1}) with significant polymer formation occurring only after 83 days (pH 7–8). This is more than 4 times longer than the duration of our experiments (20 days). Finally, in additional experiments (Supplementary Data Section 2), we observed a strong correlation between available surface area per volume unit in the reactor and precipitation rates.

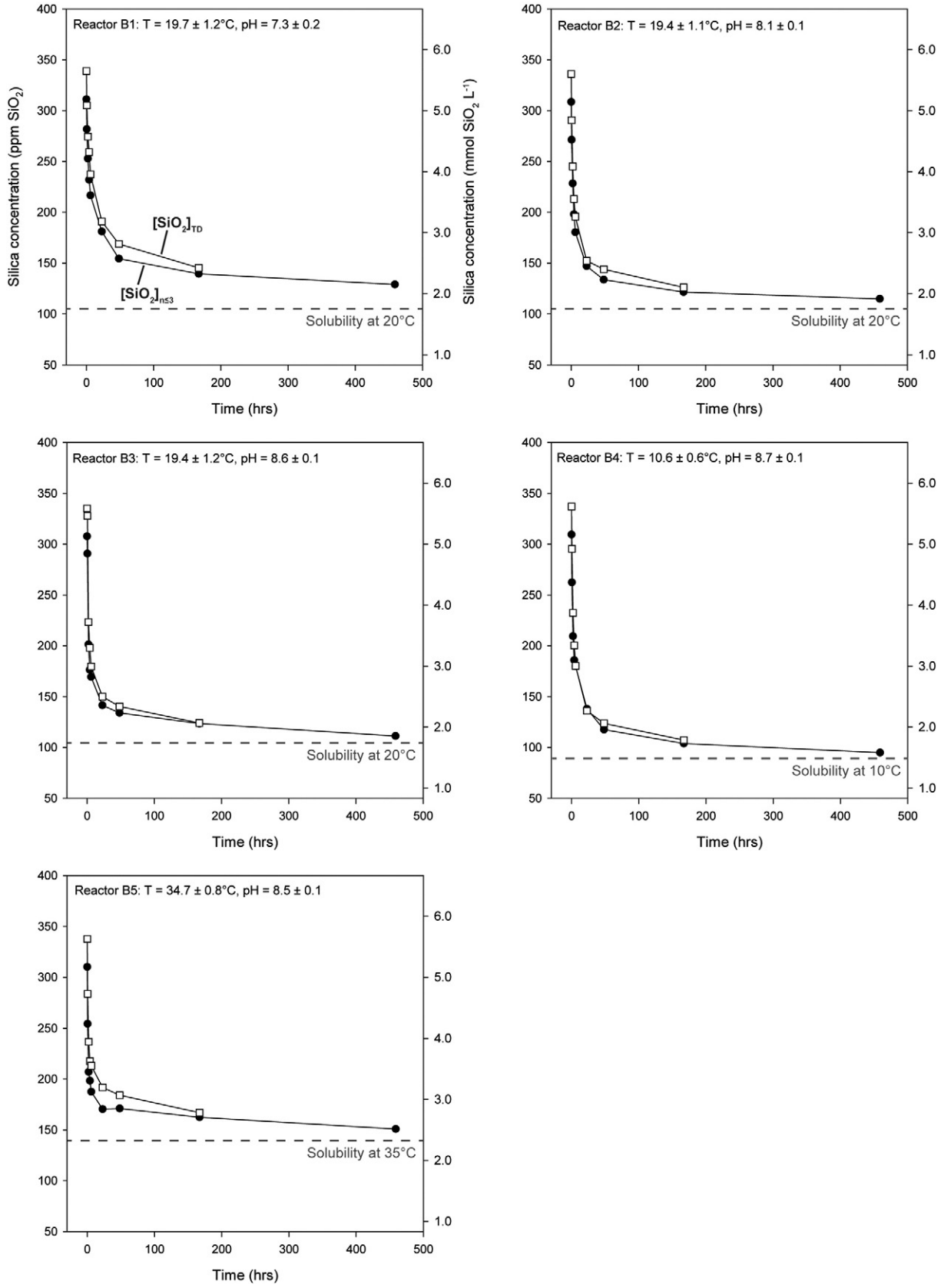

Fig. 1. Changes in the molybdate-reactive (closed circles) and total dissolved silica (open squares) concentrations in reactors over time, showing a decrease towards solubility levels towards the end of the experiment (after *ca.* 400 hours). Solubility levels are calculated from Gunnarsson and Arnórsson (2000). Errors are approximately the size of the symbols. See first panel (reactor B1) for symbol descriptions and axis titles.

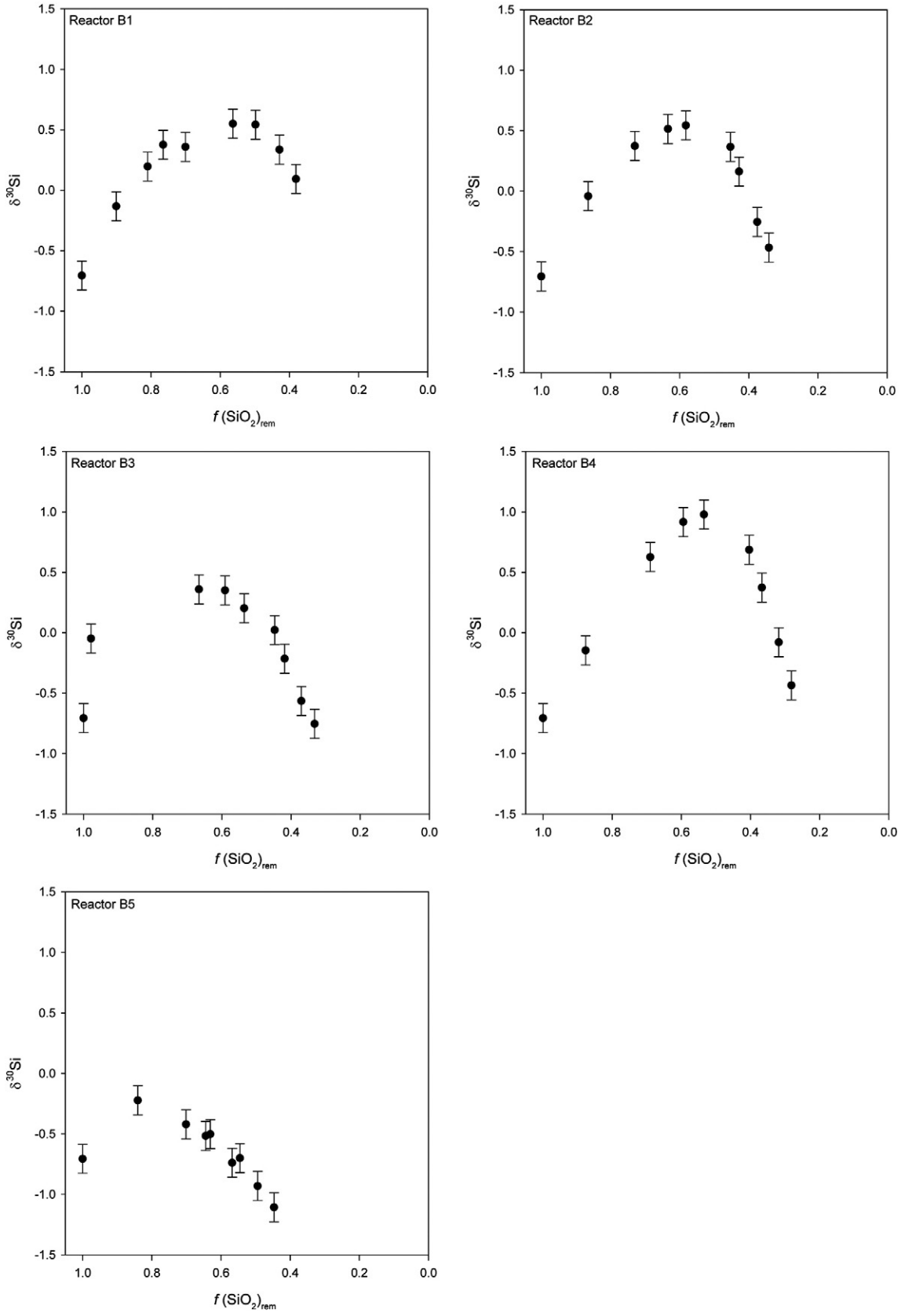

Fig. 2. Silicon isotopic compositions ($\delta^{30}Si$) of the total dissolved silica in the reactors with progressive precipitation, indicated by $f\,(SiO_2)_{rem}$. All reactors show a distinct decrease in $\delta^{30}Si_{TD}$ after $f = 0.6$, corresponding to decreasing instantaneous fractionation factors.

Table 2
Results from mass balance computations, with the mass of total dissolved silica ($mSiO_{2,TD}$) calculated from $[SiO_2]_{TD}$, the mass of precipitated silica ($mSiO_{2,\ ppt}$) calculated from mass balance, the volume-corrected surface area A and the calculated precipitation rates (R_p) in mol SiO_2 m^{-2} s^{-1}. The isotopic composition of the precipitated silica ($\delta^{30}Si_{ppt}$) is derived from isotopic mass balance (Eq. 2), and $\Delta^{30}Si$ is calculated from $\delta^{30}Si_{ppt} - \delta^{30}Si_{TD}$. Instantaneous fractionation factors (α_{inst}) are calculated as $(\delta^{30}Si_{ppt} + 1000)/(\delta^{30}Si_{TD} + 1000)$.

Sample	$mSiO_{2,TD}$	$mSiO_{2,ppt}$	A	R_p	$\delta^{30}Si_{ppt}$	$\Delta^{30}Si$	α_{inst}
	mg	mg	m^2	mol m^{-2} s^{-1}	‰	‰	
B1-1	13.4	2.2	23.0	9.87E-10	−4.10	−3.97	0.9960
B1-2	11.4	4.2	21.8	2.69E-10	−3.13	−3.33	0.9967
B1-3	9.9	5.7	20.6	1.58E-10	−2.72	−3.10	0.9969
B1-4	8.7	6.9	19.3	1.82E-10	−2.06	−2.42	0.9976
B1-5	6.8	8.8	18.1	3.55E-11	−1.63	−2.18	0.9978
B1-6	5.4	10.2	16.9	1.35E-11	−1.37	−1.92	0.9981
B1-7	4.5	11.0	15.7	2.94E-12	−1.11	−1.44	0.9986
B1-8	3.9	11.7	14.5	9.31E-13	−0.94	−1.04	0.9990
B2-1	12.9	2.5	23.0	1.21E-09	−3.76	−3.72	0.9963
B2-2	10.3	5.2	21.8	3.68E-10	−2.77	−3.14	0.9969
B2-3	8.4	7.0	20.6	2.35E-10	−2.13	−2.65	0.9974
B2-4	7.2	8.2	19.3	1.47E-10	−1.80	−2.34	0.9977
B2-5	5.5	9.9	18.1	3.21E-11	−1.26	−1.63	0.9984
B2-6	4.7	10.8	16.9	7.24E-12	−1.08	−1.24	0.9988
B2-7	3.9	11.5	15.7	2.33E-12	−0.85	−0.60	0.9994
B2-8	3.4	12.0	14.5	7.15E-13	−0.77	−0.30	0.9997
B3-1	13.8	1.6	23.0	5.96E-10	−9.38	−9.33	0.9907
B3-2	9.1	6.3	21.8	7.35E-10	−2.30	−2.66	0.9973
B3-3	7.5	7.9	20.6	1.84E-10	−1.77	−2.12	0.9979
B3-4	6.8	8.6	19.3	1.47E-10	−1.39	−1.59	0.9984
B3-5	5.3	10.1	18.1	2.37E-11	−1.07	−1.10	0.9989
B3-6	4.7	10.7	16.9	7.66E-12	−0.91	−0.70	0.9993
B3-7	4.0	11.4	15.7	2.18E-12	−0.75	−0.19	0.9998
B3-8	3.3	12.1	14.5	7.60E-13	−0.69	0.06	1.0001
B4-1	12.5	3.0	23.0	1.89E-09	−3.50	−3.35	0.9966
B4-2	9.4	6.1	21.8	5.07E-10	−2.89	−3.52	0.9965
B4-3	7.9	7.6	20.6	2.20E-10	−2.36	−3.28	0.9967
B4-4	7.2	8.3	19.3	1.49E-10	−1.97	−2.94	0.9971
B4-5	5.2	10.3	18.1	3.18E-11	−1.31	−2.00	0.9980
B4-6	4.1	11.4	16.9	8.38E-12	−1.08	−1.45	0.9985
B4-7	3.4	12.1	15.7	2.09E-12	−0.87	−0.79	0.9992
B4-8	2.8	12.6	14.5	6.97E-13	−0.76	−0.33	0.9997
B5-1	12.1	3.4	23.0	2.29E-09	−2.63	−2.40	0.9976
B5-2	9.3	6.2	21.8	4.02E-10	−1.19	−0.77	0.9992
B5-3	8.4	7.1	20.6	1.58E-10	−0.94	−0.42	0.9996
B5-4	7.5	8.0	19.3	8.28E-11	−0.91	−0.41	0.9996
B5-5	6.4	9.1	18.1	2.01E-11	−0.68	0.06	1.0001
B5-6	6.0	9.5	16.9	8.06E-12	−0.71	−0.01	1.0000
B5-7	5.3	10.2	15.7	2.53E-12	−0.60	0.33	1.0003
B5-8	4.5	11.0	14.5	9.84E-13	−0.56	0.55	1.0005

Concentrations of molybdate-reactive silica decreased faster in experiments with 10 g L^{-1} (500 m^2 L^{-1}) Aerosil OX50 particles compared to solutions with 5 g L^{-1} (250 m^2 L^{-1}) Aerosil, suggesting that precipitation occurs on the surface of the silica seeds and not as homogeneous nucleation reactions in the solution. This is also consistent with the lower acid dissociation constant for particles (pK_a ~ 7) versus monosilicic acid (pK_a ~ 9), which makes reactions on seed surfaces more favorable than reactions between two monomeric silica molecules (Iler, 1979; Fleming, 1986).

For the deposition of monomeric (and/or oligomeric) silica, a condensation reaction is required in which two silanol bonds (Si-OH) form one new siloxane bond (Si-O-Si) on the solid surface (Iler, 1979), which involves the breaking of one Si-O bond. Our isotope data support this reaction pathway, because lower bond energies for ^{28}Si-O compared to ^{30}Si-O will result in faster rupturing of the first, consistent with preferential deposition of ^{28}Si. In addition, based on large activation energies for silica precipitation, Rimstidt and Barnes (1980) suggested that this Si-O bond rupturing is the rate-determining step in the reaction, which agrees with the occurrence of a primary kinetic isotope effect. Our results also indicate that isotopic fractionation occurs primarily in the solution and not on the solid surfaces (e.g. breaking of Si-O bonds on the surface of silica seeds, or incorporation of adsorbed silica in the solid), because such surface-processes would not affect the dissolved silica pool. Thus, we argue that faster splitting of ^{28}Si-OH bonds in the dissolved silica results in a relatively ^{28}Si-enriched pool of $H_3SiO_3^+$ (or equivalent polymers with OH-groups removed from silanol bonds), and this isotopic composition is rapidly transferred to newly formed siloxane bonds after reaction with the surface of a silica particle.

Progressive precipitation of ^{28}Si-enriched silica in the closed-system reactors was expected to result in a steady increase in δ^{30}Si of the remaining dissolved silica with time following Rayleigh distillation. In contrast, our results demonstrate an opposite effect with decreasing δ^{30}S-values when more than 40% of the available silica has precipitated (Fig. 2), associated with values of instantaneous fractionation factors above 0.9971 (Table 2). We consider it unlikely that this effect is related to changes in the pathway of isotope fractionation described above, because dissociation energies of the molecules involved in the reaction are not affected by the extent of reaction (Bigeleisen, 1965), so that breaking of ^{28}Si-OH bonds should remain energetically favorable throughout the entire experiment and independent of the formation of silanol or siloxane bonds (cf. Geilert et al., 2014a).

An alternative explanation is that redissolution of silica becomes more significant towards the end of the experiment, resulting in a change from kinetically- to equilibrium-controlled precipitation when the forward precipitation rate becomes approximately equal to the backward dissolution rate (similar to observations by Oelze et al., 2014). This condition is likely reflected by dissolved silica concentrations approaching solubility levels in the reactors after *ca.* 400 hours (Fig. 1), and the decreased precipitation rates of *ca.* 10^{-13} mol SiO_2 m^{-2} s^{-1} compared to initial rates of *ca.* 10^{-9} mol SiO_2 m^{-2} s^{-1} (Table 2). Analogous to isotope effects observed during dissolution of a ^{28}Si-enriched surface layer of basalt and volcanic glass (Ziegler et al., 2005), the decrease in δ^{30}Si of the dissolved silica during the final stage of the experiments can be explained by redissolution of the ^{28}Si-enriched silica precipitate. We argue that the mechanism of isotope fractionation remained constant during the experiment, but that the measured instantaneous fractionation factor was controlled by a shifting balance between kinetic and (metastable) equilibrium processes in the batch-reactors. This is strongly similar to the link between precipitation rate and Ca isotope fractionation observed during calcite precipitation and modeled by DePaolo (2011), supporting our application of this surface-kinetic model (Section 4.1) to the fractionation of Si isotopes during silica precipitation.

5.2. Kinetic fractionation factors

The inferred transition from kinetic to equilibrium processes in the batch-reactors hampers the derivation of kinetic fractionation factors from trends in $\delta^{30}Si_{TD}$ versus f (Fig. 2), because it is unknown to what extent values of $\delta^{30}Si_{TD}$ have been suppressed by equilibrium effects after the initial stage of the experiment (between $f \approx 0.8$ and $f \approx 0.6$). Thus, if trend lines were fitted to the data to determine the magnitude of isotopic fractionation (cf. Georg et al., 2007), the resulting slopes could represent underestimates of the kinetic fractionation factors.

Our alternative method provides a more advanced approach, because the instantaneous fractionation factors calculated for the first part of the experiment are unaffected by equilibrium effects during later stages. Although model results are dependent on the calculated dissolution rates (R_b = 1.95 x 10^{-11} mol m^{-2} s^{-1} at pH 7.5; 2.24 x 10^{-11} mol m^{-2} s^{-1} at pH 8.0 and 2.63 x 10^{-11} mol m^{-2} s^{-1} at pH 8.5), the used values are based on dissolution experiments with the same batch of Aerosil OX50 amorphous silica particles (Loucaides et al., 2008) and are in good agreement with the rate of ranges reported for silica dissolution in distilled water, varying from 1.1 x 10^{-10} mol

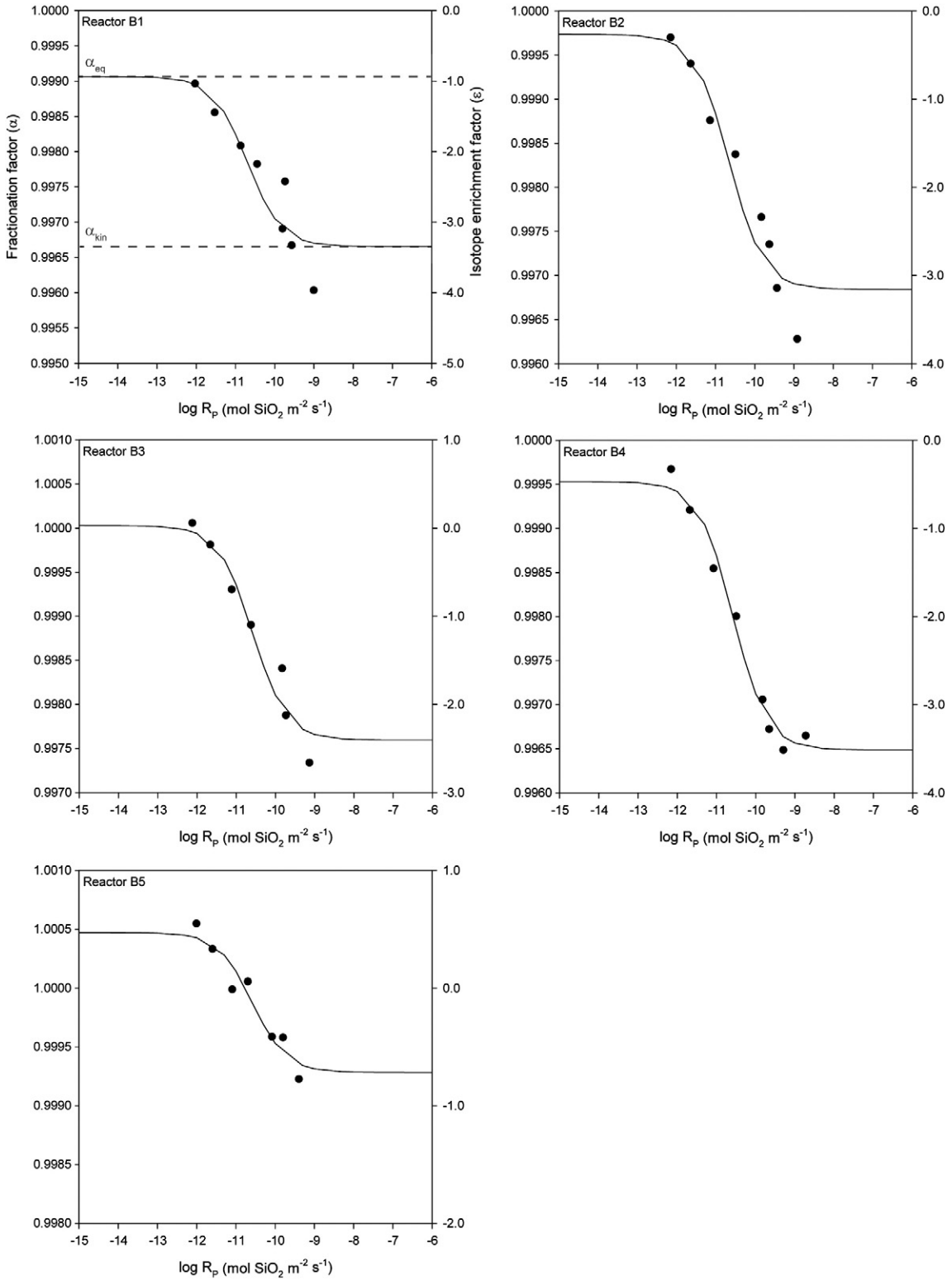

Fig. 3. Surface kinetic model curve of DePaolo (2011) fitted to the instantaneous fractionation factors against *log* precipitation rate (filled symbols). The lower limit of the curve (fastest precipitation rates) represents the kinetic fractionation factor and the upper limit (slowest precipitation rates) represents the equilibrium fractionation factor, as indicated in the first panel (reactor B1). Corresponding isotope enrichment factors (ε) are given on the secondary axis.

SiO_2 m^{-2} s^{-1} at pH 13 and room temperature to 4.4 x 10^{-12} mol SiO_2 m^{-2} s^{-1} at pH 5.7 and 40–60 °C (Rimstidt and Barnes, 1980; Mazer and Walther, 1994; Seidel et al., 1997; Icenhower and Dove, 2000).

The modeled kinetic isotopic enrichment factors range from −0.7 ± 0.2‰ to −3.5 ± 0.2‰, and are larger than isotope effects of −0.4 to −1.0‰ reported from batch-reactor experiments by Li et al. (1995). In view of the changing instantaneous fractionation observed in our experiments, we argue that these data from Li et al. (1995) represent underestimates of the kinetic isotope effects due to interaction of equilibrium processes. Silica precipitation was nearly complete in their experiments ($f \rightarrow 0$) and the isotopic composition of dissolved and precipitated silica was measured 24–72 hours after the start of

Table 3
Model results derived from fitting the DePaolo (2011) model curve to plots of instantaneous fractionation factors versus precipitation rate, using backward dissolution rates (R_b) that were extrapolated from rates of Aerosil OX50 dissolution measured at pH 6.3 and pH 8.1 (Loucaides et al., 2008). Goodness of fit is given as R^2, and errors on kinetic (α_{kin}) and equilibrium (α_{eq}) fractionation factors are given as 95% confidence intervals ($z_{2.5}$). Isotope enrichment factors (ε_{kin} and ε_{eq}) are calculated as $\varepsilon = 1000 \ln\alpha$.

Reactor	R_b	R^2	n	α_{kin}	$z_{2.5}$	ε_{kin}	α_{eq}	$z_{2.5}$	ε_{eq}
	mol m^{-2} s^{-1}					‰			‰
B1	1.95E-11	0.84	8	0.9967	0.0005	-3.4 ± 0.5	0.9991	0.0016	-0.9 ± 1.6
B2	2.24E-11	0.92	8	0.9968	0.0005	-3.2 ± 0.5	0.9997	0.0014	-0.3 ± 1.4
B3	2.63E-11	0.94	7	0.9976	0.0004	-2.4 ± 0.4	1.0000	0.0011	0.0 ± 1.1
B4	2.63E-11	0.98	8	0.9965	0.0002	-3.5 ± 0.2	0.9995	0.0007	-0.5 ± 0.7
B5	2.63E-11	0.92	7	0.9993	0.0002	-0.7 ± 0.2	1.0005	0.0006	0.5 ± 0.6

the experiment, suggesting that redissolution processes were probably as important as in our batch-reactors. This also agrees with their derivation of the largest fractionation factor (0.9990) for the experiment with the lowest extent of silica precipitation ($f = 0.547$), i.e. the experiment that is least equilibrium-dominated. Similar influences from equilibrium fractionation could explain the smaller enrichment factors obtained from flow-through reactor experiments at steady state, which ranged from −2.1‰ at 10 °C to −1.0‰ at 30 °C (Geilert et al., 2014a). Nevertheless, our results do agree with the temperature-dependency of Si isotope fractionation observed by Geilert (2014a), showing a decrease in fractionation from -3.5 ± 0.2‰ at 10 °C, to -2.4 ± 0.4‰ at 20 °C and -0.7 ± 0.2‰ at 35 °C (all at pH 8.5). Unlike equilibrium isotope effects where the vibrational energy of molecules controls the magnitude of isotope fractionation (Urey, 1947), the temperature-dependency of the kinetic fractionation factor likely reflects how the kinetics of the rate-determining step during silica precipitation are a function of temperature. Moreover, comparison of results from reactors at 20 °C and different pH-values also demonstrates smaller kinetic isotope fractionation at pH 8.5 than at pH 7.5–8.0 (Table 3). The origin of this pH-dependency may be related to an increase in deprotonated monomeric silica molecules ($H_3SiO_4^-$) above pH 8 (Iler, 1979), affecting the kinetics of the Si-OH bond-breaking step.

5.3. Equilibrium fractionation factors

Although full isotopic equilibrium is generally difficult to obtain in low-temperature systems, dissolved silica concentrations and calculated reaction rates suggest that a metastable equilibrium is approached in our batch-reactors at the end of the experiment (see discussion in Section 5.1). Smaller magnitudes of instantaneous isotope effects (i.e. $\alpha_{inst} \rightarrow 1.000$) obtained for this stage (Table 2) are also consistent with a change towards equilibrium-dominated isotope fractionation, as equilibrium fractionation factors have been suggested to be close to unity for the silica-water system from δ^{30}Si-values measured in equilibrated geothermal systems (Douthitt, 1982). Our regression results suggest that the magnitude of equilibrium isotope enrichment factors between metastable amorphous silica and dissolved silica ranges from -0.5 ± 0.7‰ at 10 °C, to 0.0 ± 1.1‰ at 20 °C and $+0.5 \pm 0.6$‰ at 35 °C (all at pH 8.5, Table 3), consistent with the inverse relationship between temperature and isotope fractionation in equilibrium processes (Urey, 1947; Bigeleisen, 1965). Results also suggest larger equilibrium fractionation with decreasing pH, which may be explained by faster and more efficient redissolution rates at higher pH-values. However, it should be noted that uncertainties are larger for the equilibrium fractionation factors than for the kinetic effects.

Unfortunately, comparison of our experimentally-derived equilibrium fractionation factors with theoretical values based on statistical thermodynamics is hampered by the lack of data for the silica-water system (e.g. Méheut et al., 2007, 2009). In addition, general considerations such as that the magnitude of equilibrium fractionation increases with the degree of polymerization of SiO_4 tetrahedra in the silicate structure (Grant, 1953) are not applicable to the amorphous silica precipitating in our batch-reactors. Novel computations of equilibrium silicon isotope effects between dissolved and amorphous silica at low temperatures are thus essential for the validation of experimental results.

5.4. Silicon isotope fractionation during chert formation

Significant differences in the magnitude of kinetic and equilibrium fractionation factors and their dependency on temperature, as observed in this study and by Geilert et al. (2014a), suggest that the kinetic regime at which silica precipitates exerts an important control on the silicon isotope fractionation expressed in non-biogenic chert deposits. Below, we discuss the implications of this result for the silicon isotopic composition of cherts formed in different environmental settings.

5.4.1. Isotope fractionation during non-biogenic silica precipitation

Throughout geological history, the formation of non-biogenic silica deposits is related to the deposition of siliceous sinters formed near hot springs, geysers and submarine hydrothermal chimneys, primary chemical precipitates formed in lacustrine and marine settings, and replacement cherts and silcretes formed by silicification of precursor rocks (Boggs, 2009). Environmental conditions, such as the temperature and degree of silica oversaturation, are likely to be different in each of these systems, thus affecting the fractionation of silicon isotopes during silica precipitation. Most important, the small magnitudes of equilibrium fractionation factors found in this study imply that effective silicon isotope fractionation in natural systems will be limited, unless the precipitation reaction remains unidirectional and kinetic isotope effects are preserved (cf. Mg isotopes during magnesite precipitation; Pearce et al., 2012). In hydrothermal settings, the establishment of equilibrium between dissolved and precipitated silica at 0–300 °C was shown to be inversely related to the rate constant for precipitation reactions, which in turn depends on the temperature and extent of the system (Rimstidt and Barnes, 1980). For example, fast precipitation at high temperatures (200–300 °C) results in equilibration times of a few hours to a few weeks, whereas equilibration is considerably slower in low-temperature systems (20–100 °C) where significant degrees of silica oversaturation can be maintained for relatively long periods of time. In addition, dissolved and precipitated silica will equilibrate significantly less in systems with large fractures and an unrestricted fluid flow to the surface compared to systems where fluids slowly percolate through rocks (Rimstidt and Barnes, 1980).

Based on these kinetic conditions, we argue that the small equilibrium isotope fractionation factors are applicable to silica that is deposited at depth in high-temperature hydrothermal systems, and to low-temperature deposits that are formed by the silicification and replacement of precursor rocks. Limited isotope fractionation in these systems is consistent with silicon isotope ratios measured in microcrystalline quartz in a silicified marine sandstone ($\delta^{30}Si = +0.2 \pm 0.6$‰; Basile-Doelsch et al., 2005) that are only slightly fractionated compared to potential sources of the silicon, i.e. primary quartz in the sandstone ($\delta^{30}Si = 0.3 \pm 0.9$‰; Basile-Doelsch et al, 2005) or seawater ($+1.1 \pm 0.3$‰; De La Rocha et al., 2000). Likewise, the isotopic composition of dissolved silica in hydrothermal fluids ($+0.2 \pm 0.2$‰; Douthitt, 1982) is similar to δ^{30}Si-values measured in silica in Chinese disseminated gold deposits of deep hydrothermal origin ($\delta^{30}Si =$

−0.4 to +0.5‰; Xianfan et al, 1998), as well as chalcedony formed at depth in the geothermal area of Steamboat Springs, Nevada that shows oxygen isotopic evidence for equilibration ($\delta^{30}Si = +0.2 \pm 0.5‰$; Douthitt, 1982).

Alternatively, in surface environments, where silica precipitates from strongly oversaturated solutions into cooler streams or seawater, reactions are more likely to be unidirectional with no significant backward dissolution, resulting in the potential preservation of larger kinetic isotope effects in the rock record. This was, for example, observed by Geilert (2013) at the Geysir geothermal field in Iceland, where silica deposits in stream beds had the lowest δ^{30}Si-values (down to −4.0‰) where cooling was most advanced, i.e. at the largest distance from the hot-spring sources. Similarly, large isotope effects during low-temperature sinter formation are consistent with strongly ^{30}Si-depleted isotopic compositions (δ^{30}Si-values down to −3.1‰) for silica deposits in geothermal fields of New Zealand and Yellowstone (USA) reported by Douthitt (1982).

Although our experimental results are, in principle, only applicable to pure silica-water systems, similar signs and magnitudes of fractionation factors were found during silica adsorption on Fe-oxides (Delstanche et al., 2009), supporting a comparable reaction mechanism in the presence of iron-rich phases. Remarkably, Oelze et al. (2014) reported an equivalent change from kinetic to equilibrium fractionation during silica absorption on Al-oxides, and kinetic fractionation factors that were of similar magnitude to those in our pure silica-water system. This suggests that our model with system-dependent expressions of silicon isotope effects is also likely to be valid for systems with additional mineral phases.

5.4.2. Silicon isotope variations in Archean chert deposits

Although diagenesis may have affected primary silicon isotope compositions of Precambrian chert deposits (Marin et al., 2010; Marin-Carbonne et al., 2011), isotopic variations at several localities correspond to different Al_2O_3-contents and rare earth element patterns (e.g. Van den Boorn et al., 2007; Van den Boorn et al., 2010; Abraham et al., 2011; Marin-Carbonne et al., 2012; Geilert et al., 2014b), indicating that (near-)primary signatures are often preserved. S-cherts show a limited range in δ^{30}Si-values from +0.1 to +1.1‰ with variable Al_2O_3-contents, and have been linked to the silicification of volcanic-sedimentary precursor rocks (Van den Boorn et al., 2007, 2010; Abraham et al., 2011). In contrast, C-cherts contain very little Al_2O_3 and show a larger range in δ^{30}Si-values that extend to more ^{30}Si-depleted compositions, e.g. down to −3.7‰ for Eoarchean banded iron formations from Isua, Greenland (Heck et al., 2011), −2.4‰ for Paleoarchean chert from the Pilbara craton, Western Australia (Van den Boorn et al., 2007, 2010), −2.6‰ for Paleoarchean chert from South Africa and Zimbabwe (Steinhoefel et al., 2009; Marin-Carbonne et al., 2011; Geilert et al., 2014b) and −4.3‰ for Proterozoic banded iron formations from Western Australia (Chakrabarti et al., 2012). The origin of these cherts has been linked to chemical precipitation of silica from mixtures of hydrothermal fluids and seawater (e.g. Van den Boorn et al., 2007).

Whereas different sources of silica can explain much of the silicon isotope variation in S-cherts and C-cherts (Van den Boorn et al., 2007, 2010), our findings indicate that the conditions and mechanism of silica precipitation could have been an additional control on isotope ratios preserved in ancient chert deposits. Most importantly, our results suggest that isotopic fractionation was dependent on the precipitation regime, and that different fractionation factors applied to the silicification of precursor rocks and the formation of orthochemical cherts. Slow percolation of silica-rich seawater through basalts and volcanic-sedimentary rocks may have facilitated chemical and isotopic equilibrium between dissolved and precipitated silica in pore spaces, similar to modern replacement cherts. With minimal equilibrium isotope fractionation, the δ^{30}Si-value of S-cherts should thus have been determined predominantly by the isotopic composition of the source of the dissolved silica, that of the precursor rock and the ratio between silica precipitate and precursor, assuming that any later diagenetic or metamorphic alteration can be excluded. Hence, if Archean seawater had a δ^{30}Si-value of ~1‰ (Marin-Carbonne et al., 2012), the most ^{30}Si-enriched S-cherts ($\delta^{30}Si = +1.1‰$) are consistent with little or no isotope effects during silicification (Van den Boorn et al., 2007, 2010; Abraham et al., 2011). Less ^{30}Si-enriched S-cherts can be explained by a larger contribution of silicon from precursor rocks, which commonly have slightly negative δ^{30}Si-values, e.g. $\delta^{30}Si = -0.29 \pm 0.08$ ‰ for mafic to ultramafic rocks (Savage et al., 2010), and $\delta^{30}Si = -0.25 \pm 0.16‰$ for the average upper continental crust (Savage et al., 2013). Such a scenario agrees with isotope data from S-cherts at Kitty's Gap, Western Australia, where the most positive δ^{30}Si-values were found in strongly silicified fine-grained ash layers and less silicified rocks showed lower δ^{30}Si-values (Van den Boorn et al., 2010).

On the other hand, orthochemical chert deposits likely formed under non-equilibrium conditions when silica precipitated from oversaturated fluid mixtures at relatively low ambient seawater temperatures (Van den Boorn et al., 2007, 2010), presumably without significant backward dissolution. The larger kinetic isotope effect inferred for this pathway of chert formation is consistent with the strongly negative δ^{30}Si-values reported for C-cherts, which are often considerably lower than the value of −0.3‰ of modern deep-sea hydrothermal fluids (De La Rocha et al., 2000), assuming that this was similar in Precambrian times. Less negative δ^{30}Si-values for orthochemical cherts suggest an increased proportion of seawater-derived silica to the mixture from which the chert precipitated, shifting the composition of the dissolved silica pool towards more positive values. Alternatively, based on our results, these less negative values can also reflect precipitation conditions favorable for isotopic fractionation closer to equilibrium. These apparent relationships between the magnitude of isotope fractionation during silica precipitation, different mixing ratios of hydrothermal and seawater silica, and possible variations in the kinetic regime explain why the range in δ^{30}Si-values is larger for C-cherts than for S-cherts.

6. Summary and conclusions

This study reports on the stable silicon isotope fractionation during chemical precipitation of silica in batch-reactor experiments at low temperature (10–35 °C) and near-neutral pH (7.5–8.5), as analogue for non-biogenic chert formation. We derived magnitudes of kinetic and equilibrium fractionation factors based on the surface kinetic model of DePaolo (2011). Input parameters for this model are our measured δ^{30}Si-values of the dissolved silica and instantaneous fractionation factors calculated from a mass balance model. Our main findings and conclusions are summarized below.

- Kinetic silicon isotope effects during silica precipitation at pH 8.5 are described by fractionation factors ranging from 0.9965 at 10 °C, to 0.9976 at 20 °C and 0.9993 at 35 °C. In contrast, equilibrium isotope effects are smaller and range from 0.9995 at 10 °C, to 1.0000 at 20 °C and 1.0005 at 35 °C. Fractionation factors are slightly larger at lower pH (7.5–8.0).
- Similar to Ca and Mg isotope fractionation during calcite and magnesite precipitation (DePaolo, 2011; Pearce et al., 2012), our results imply that the large kinetic isotope effects will only be expressed in natural systems where dissolved and precipitated silica are not in equilibrium. Thus, the expression of isotope effects during chert formation is strongly dependent on the degree of (metastable) equilibrium in the silica-water system.
- Slow percolation of siliceous fluids through pore spaces during the silicification of modern sandstone deposits or Archean silicified volcanic-sedimentary rocks (S-chert) presumably facilitates equilibrium between dissolved and precipitated silica, resulting in small isotopic fractionation. Therefore, no Rayleigh fractionation is required

to explain the formation of S-chert with $\delta^{30}Si = +1.1$ from Archean seawater with $\delta^{30}Si$ ~ 1‰ (cf. Van den Boorn et al., 2010; Abraham et al., 2011; Heck et al., 2011; Chakrabarti et al., 2012).
- Negative $\delta^{30}Si$-values observed in modern geothermal sinter deposits (down to −4.0‰) and Archean orthochemical cherts (down to −4.3‰) can be explained by rapid precipitation of silica from oversaturated solutions that is dominated by kinetic isotope fractionation. Isotope effects found in natural samples are consistent with experimentally-derived magnitudes of kinetic fractionation factors, eliminating the requirement of sequential fractionation processes (cf. Heck et al., 2011; Marin-Carbonne et al., 2011).
- The temperature-dependency of fractionation factors found in this study supports experimental findings by Geilert et al. (2014a) and indicates that silicon isotope fractionation during silica precipitation is only significant at low temperatures (<100 °C).

Our work implies that the kinetic regime at which the silica was precipitated provides an important additional control on the silicon isotopic composition of chert deposits. This potentially complicates the application of the silicon isotope proxy to ancient chert deposits to determine conditions in the earliest marine environments, and calls for careful assessment of the depositional environment of these cherts based on other data than silicon isotope ratios alone (cf. Marin-Carbonne et al., 2012).

Acknowledgements

We thank Pieter Kleingeld, Helen de Waard, Bas van der Wagt and Richard Smeets for inventive and skillful technical support in the lab. Socratis Loucaides is thanked for providing us with Aerosil silica powders, and we are grateful to Rob Govers for his help with mathematical equations and data fitting. We thank three anonymous reviewers and Michael Böttcher for constructive reviews that helped to improve the manuscript. This project was partly financially supported by the Netherlands Organization for Scientific Research (NWO), project no. 819.01.005. The MC-ICP-MS facility was supported by a grant (175.107.404.01) from the Netherlands Organization for Scientific Research (NWO-ALW).

Appendix A. Supplementary data

Supplementary data to this article can be found online at http://dx.doi.org/10.1016/j.chemgeo.2015.02.038.

References

Abraham, K., et al., 2011. Coupled silicon-oxygen isotope fractionation traces Archaean silicification. Earth Planet. Sci. Lett. 301 (1–2), 222–230.
Basile-Doelsch, I., Meunier, J.D., Parron, C., 2005. Another continental pool in the terrestrial silicon cycle. Nature 433, 399–402.
Bigeleisen, J., 1965. Chemistry of Isotopes: Isotope chemistry has opened new areas of chemical physics, geochemistry, and molecular biology. Science 147 (3657), 463–471.
Boggs, S., 2009. Evaporites, cherts, iron-rich sedimentary rocks, and phosphorites. Petrology of sedimentary rocks. Cambridge University Press, pp. 461–526.
Cardinal, D., Alleman, L.Y., De Jong, J., Ziegler, K., André, L., 2003. Isotopic composition of silicon measured by multicollector plasma source mass spectrometry in dry plasma mode. J. Anal. At. Spectrom. 18, 213–218.
Chakrabarti, R., Knoll, A.H., Jacobsen, S.B., Fischer, W.W., 2012. Si isotope variability in Proterozoic cherts. Geochim. Cosmochim. Acta 91, 187–201.
Conrad, C.F., et al., 2007. Modeling the kinetics of silica nanocolloid formation and precipitation in geologically relevant aqueous solutions. Geochim. Cosmochim. Acta 71, 531–542.
De La Rocha, C.L., 2002. Measurement of silicon stable isotope natural abundances via multicollector inductively coupled plasma mass spectrometry (MC-ICP-MS). Geochem. Geophys. Geosyst. 3 (8), 1045.
De La Rocha, C.L., 2006. Opal-based isotopic proxies of paleoenvironmental conditions. Glob. Biogeochem. Cycles 20 (4).
De La Rocha, C.L., Bickle, M.J., 2005. Sensitivity of silicon isotopes to whole-ocean changes in the silica cycle. Mar. Geol. 217, 267–282.
De La Rocha, C.L., Brzezinski, M.A., DeNiro, M.J., 1997. Fractionation of silicon isotopes by marine diatoms during biogenic silica formation. Geochim. Cosmochim. Acta 61, 5051–5056.
De La Rocha, C.L., Brzezinski, M.A., DeNiro, M.J., Shemeshk, A., 1998. Silicon-isotope composition of diatoms as an indicator of past oceanic change. Nature 395, 680–683.
De La Rocha, C.L., Brzezinski, M.A., DeNiro, M.J., 2000. A first look at the distribution of the stable isotopes of silicon in natural waters. Geochim. Cosmochim. Acta 64, 2467–2477.
Delstanche, S., et al., 2009. Silicon isotopic fractionation during adsorption of aqueous monosilicic acid onto iron oxide. Geochim. Cosmochim. Acta 73 (4), 923–934.
Demarest, M.S., Brzezinski, M.A., Beucher, C.P., 2009. Fractionation of silicon isotopes during biogenic silica dissolution. Geochim. Cosmochim. Acta 73 (19), 5572–5583.
DePaolo, D.J., 2004. Calcium isotopic variations produced by biological, kinetic, radiogenic and nucleosynthetic processes. In: Johnson, C.M., Beard, B.L., Albarede, F. (Eds.), Geochemistry of non-traditional stable isotopes. Reviews in Mineralogy and Geochemistry. Mineralogical Society of America.
DePaolo, D.J., 2011. Surface kinetic model for isotopic and trace element fractionation during precipitation of calcite from aqueous solutions. Geochim. Cosmochim. Acta 75 (4), 1039–1056.
Ding, T.P., et al., 1996. Silicon isotope geochemistry. Geological Publishing, Beijing.
Douthitt, C.B., 1982. The geochemistry of the stable isotopes of silicon. Geochim. Cosmochim. Acta 46, 1449–1458.
Egan, K.E., et al., 2012. Diatom silicon isotopes as a proxy for silicic acid utilisation: A Southern Ocean core top calibration. Geochim. Cosmochim. Acta 96, 174–192.
Fleming, B.A., 1986. Kinetics of reaction between silicic acid and amorphous silica surfaces in NaCl solutions. J. Colloid Interface Sci. 110, 40–64.
Geilert, S., 2013. Silicon isotope fractionation during silica precipitation from hot-spring waters: evidence from the Geysir hydrothermal field, Iceland. Silicon isotope fractionation during silica precipitation from aqueous solutions - Experimental and field evidence. 48. Utrecht Studies in Earth Sciences, Utrecht.
Geilert, S., Vroon, P.Z., Roerdink, D.L., Van Cappellen, P., van Bergen, M.J., 2014a. Silicon isotope fractionation during abiotic silica precipitation at low temperatures: Inferences from flow-through experiments. Geochim. Cosmochim. Acta 142, 95–114.
Geilert, S., Vroon, P.Z., van Bergen, M.J., 2014b. Silicon isotopes and trace elements in chert record early Archean basin evolution. Chem. Geol. 386, 133–142.
Georg, R.B., Reynolds, B.C., West, A.J., Burton, K.W., Halliday, A.N., 2007. Silicon isotope variations accompanying basalt weathering in Iceland. Earth Planet. Sci. Lett. 261, 476–490.
Grant, F.S., 1953. The geological significance of variations in the abundances of the isotopes of silicon in rocks. Geochim. Cosmochim. Acta 5, 225–242.
Gunnarsson, I., Arnórsson, S., 2000. Amorphous silica solubility and the thermodynamic properties of H_4SiO_4 in the range of 0 to 350°C at P_{sat}. Geochim. Cosmochim. Acta 64, 2295–2307.
Heck, P.R., et al., 2011. SIMS analyses of silicon and oxygen isotope ratios for quartz from Archean and Paleoproterozoic banded iron formations. Geochim. Cosmochim. Acta 75 (20), 5879–5891.
Icenhower, J.P., Dove, P.M., 2000. The dissolution kinetics of amorphous silica into sodium chloride solutions: effects of temperature and ionic strength. Geochim. Cosmochim. Acta 64 (24), 4193–4203.
Icopini, G.A., Brantley, S.L., Heaney, P.J., 2005. Kinetics of silica oligomerization and nanocolloid formation as a function of pH and ionic strength at 25C. Geochim. Cosmochim. Acta 69, 293–303.
Iler, R.K., 1979. The chemistry of silica. John Wiley and Sons.
Li, Y., Ding, T., Wan, D., 1995. Experimental study of silicon isotope dynamic fractionation and its application in geology. Chin. J. Geochem. 14 (3), 212–219.
Loucaides, S., Cappellen, P.V., Behrends, T., 2008. Dissolution of biogenic silica from land to ocean: role of salinity and pH. Limnol. Oceanogr. 53 (4), 1614.
Marin, J., Chaussidon, M., Robert, F., 2010. Microscale oxygen isotope variations in 1.9Ga Gunflint cherts: Assessments of diagenesis effects and implications for oceanic paleotemperature reconstructions. Geochim. Cosmochim. Acta 74 (1), 116–130.
Marin-Carbonne, J., Chaussidon, M., Boiron, M.C., Robert, F., 2011. A combined in situ oxygen, silicon isotopic and fluid inclusion study of a chert sample from Onverwacht Group (3.35Ga, South Africa): New constraints on fluid circulation. Chem. Geol. 286 (3–4), 59–71.
Marin-Carbonne, J., Chaussidon, M., Robert, F., 2012. Micrometer-scale chemical and isotopic criteria (O and Si) on the origin and history of Precambrian cherts: Implications for paleo-temperature reconstructions. Geochim. Cosmochim. Acta 92, 129–147.
Marin-Carbonne, J., Robert, F., Chaussidon, M., 2014. The silicon and oxygen isotope compositions of Precambrian cherts: A record of oceanic paleo-temperatures? Precambrian Res. 247, 223–234.
Mazer, J.J., Walther, J.V., 1994. Dissolution kinetics of silica glass as a function of pH between 40 and 85 °C. J. Non-Cryst. Solids 170 (1), 32–45.
Méheut, M., Lazzeri, M., Balan, E., Mauri, F., 2007. Equilibrium isotopic fractionation in the kaolinite, quartz, water system: Prediction from first-principles density-functional theory. Geochim. Cosmochim. Acta 71 (13), 3170–3181.
Méheut, M., Lazzeri, M., Balan, E., Mauri, F., 2009. Structural control over equilibrium silicon and oxygen isotopic fractionation: A first-principles density-functional theory study. Chem. Geol. 258 (1–2), 28–37.
Oelze, M., von Blanckenburg, F., Hoellen, D., Dietzel, M., Bouchez, J., 2014. Si stable isotope fractionation during adsorption and the competition between kinetic and equilibrium isotope fractionation: Implications for weathering systems. Chem. Geol. 380, 161–171.
Pearce, C.R., Saldi, G.D., Schott, J., Oelkers, E.H., 2012. Isotopic fractionation during congruent dissolution, precipitation and at equilibrium: Evidence from Mg isotopes. Geochim. Cosmochim. Acta 92, 170–183.
Plettinck, S., Chou, L., Wollast, R., 1994. Kinetics and mechanisms of dissolution of silica at room temperature and pressure. Mineral. Mag. 58A, 728–729.

Rimstidt, J.D., Barnes, H.L., 1980. The kinetics of silica-water reactions. Geochim. Cosmochim. Acta 44, 1683–1699.
Robert, F., Chaussidon, M., 2006. A paleotemperature curve for the Precambrian oceans based on silicon isotopes in cherts. Nature 443, 969–972.
Rothbaum, H.P., Rohde, A.G., 1979. Kinetics of silica polymerization and deposition from dilute solutions between 5 and 180°C. J. Colloid Interface Sci. 71, 533–559.
Savage, P.S., Georg, R.B., Armytage, R.M.G., Williams, H.M., Halliday, A.N., 2010. Silicon isotope homogeneity in the mantle. Earth Planet. Sci. Lett. 295 (1–2), 139–146.
Savage, P.S., Georg, R.B., Williams, H.M., Halliday, A.N., 2013. The silicon isotope composition of the upper continental crust. Geochim. Cosmochim. Acta 109, 384–399.
Seidel, A., Löbbus, M., Vogelsberger, W., Sonnefeld, J., 1997. The kinetics of dissolution of silica "Monospher" into water at different concentrations of background electrolyte. Solid State Ionics 101-103 (Part 2), 713–719.
Siever, R., 1991. The silica cycle in the Precambrian. Geochim. Cosmochim. Acta 56, 3265–3272.
Skulan, J.L., Beard, B.L., Johnson, C.M., 2002. Kinetic and equilibrium Fe isotope fractionation between aqueous Fe(III) and hematite. Geochim. Cosmochim. Acta 66, 2995–3015.
Steinhoefel, G., Horn, I., von Blanckenburg, F., 2009. Micro-scale tracing of Fe and Si isotope signatures in banded iron formation using femtosecond laser ablation. Geochim. Cosmochim. Acta 73 (18), 5343–5360.
Sutton, J.N., Varela, D.E., Brzezinski, M.A., Beucher, C.P., 2013. Species-dependent silicon isotope fractionation by marine diatoms. Geochim. Cosmochim. Acta 104, 300–309.
Tréguer, P., et al., 1995. The silica balance in the world ocean: A reestimate. Science 268 (5209), 375–379.
Urey, H.C., 1947. The thermodynamic properties of isotopic substances. J. Chem. Soc. 562–581.
Van den Boorn, S.H.J.M., et al., 2006. Determination of silicon isotope ratios in silicate materials by high-resolution MC-ICP-MS using a sodium hydroxide sample digestion method. J. Anal. At. Spectrom. 21, 734–742.
Van den Boorn, S.H.J.M., Van Bergen, M.J., Nijman, W., Vroon, P.Z., 2007. Dual role of seawater and hydrothermal fluids in Early Archaean chert formation: evidence from silicon isotopes. Geology 35 (10), 939–942.
Van den Boorn, S.H.J.M., van Bergen, M.J., Vroon, P.Z., de Vries, S.T., Nijman, W., 2010. Silicon isotope and trace element constraints on the origin of ~3.5 Ga cherts: Implications for Early Archaean marine environments. Geochim. Cosmochim. Acta 74 (3), 1077–1103.
Weres, O., Yee, A., Tsao, L., 1981. Kinetics of silica polymerization. J. Colloid Interface Sci. 84, 379–402.
Wirth, G.S., Gieskes, J.M., 1979. The initial kinetics of the dissolution of vitreous silica in aqueous media. J. Colloid Interface Sci. 68 (3), 492–500.
Xianfan, L., Shijun, N., Qiuxia, L., Jingfu, J., Laimin, Z., 1998. Silicon isotope geochemistry of micro-fine disseminated gold deposits in SW Guizhou and NW Guangxi, China. Chin. J. Geochem. 17 (3), 249–257.
Zambardi, T., Poitrasson, F., 2011. Precise determination of silicon isotopes in silicate rock reference materials by MC-ICP-MS. Geostand. Geoanalytical Res. 35 (1), 89–99.
Ziegler, K., Chadwick, O.A., Brzezinski, M.A., Kelly, E.F., 2005. Natural variations of $\delta^{30}Si$ ratios during progressive basalt weathering, Hawaiian Islands. Geochim. Cosmochim. Acta 69, 4597–4610.